COVARIANCE SIZE AND THE BREAKDOWN OF GAUSSIANITY IN GEO UNCERTAINTY PREDICTIONS

S. K. Flegel, M. Möckel, and J. Bennett

Space Environment Research Centre (SERC), Weston Creek, ACT 2611, Australia, Email: {svenflegel, marekmoeckel, jamesbennett}@serc.org.au

ABSTRACT

The accurate representation of the orbital state uncertainty is important, for example, to realistically estimate the risk of collision. Efficient algorithms exist especially for the case of Gaussian uncertainty distributions with other restrictions such as short encounter times. The current paper investigates the time frame for which the uncertainty volume of objects in GEO may be assumed to be Gaussian and how it is affected by the size of initial variances. The analysis begins with the best-case scenario of unperturbed two-body motion where the Gaussianity is preserved the longest. This is followed up by simulations employing a high accuracy numerical integrator considering a more complete perturbation force model with higher order gravitational harmonics, sun and moon gravitational effects, and direct solar radiation pressure to obtain a more realistic estimate over a wide range of variances. A comparison with realistic uncertainties of GEO object states concludes the analysis and insights are gained into the applicability and limitations of available data.

Key words: covariance; uncertainty prediction; GEO; Gaussianity; Henze-Zirkler.

1. INTRODUCTION

In the prediction of the uncertainty volume surrounding an object's state, an important question is currently being asked: "How long does the uncertainty volume which is described by the covariance matrix take to become non-Gaussian?" The short answer: Immediately after the initial epoch. The long answer: Mathematically, the normal distribution used to describe the uncertainty extends to infinity. With this picture in mind it becomes easy to imagine that those parts of the uncertainty space which are very close to the Earth's surface for instance will be distorted differently than those which extend out into space. The uncertainty space in its entirety therefore cannot remain Gaussian for any significant amount of time. The uncertainty volume close to the object itself on the other hand may very well remain Gaussian to within machine precision for non-negligible time frames. The same can be shown to be true even for the simple, unperturbed two-body case. Figure 1 is produced by predicting an object's position using only uncertainty in two dimensions of the position in ECI coordinates. The blue lines are made up of individual particles created at the σ-lines 1 to 10 at the initial epoch where Gaussianity is given by definition. The red lines are made up of the same particles after propagation to $t_1 = t_0 + \Delta t$. To ease comparison of the two samples, the particle positions are transformed into Mahalanobis space. Within this space, particle distances from the mean are given in multiples of standard deviations (more detail on this is provided in Section 3.3). At t_1, it can be seen that while Gaussianity close to the state mean is still intact, this is not the case at $10\,\sigma$. Obviously, the initial question is not complete, if the basic concept of the covariance matrix is left untouched. Before addressing it as it stands, we must therefore answer the question as to which confidence level (how many standard deviations from the mean) we are interested in.

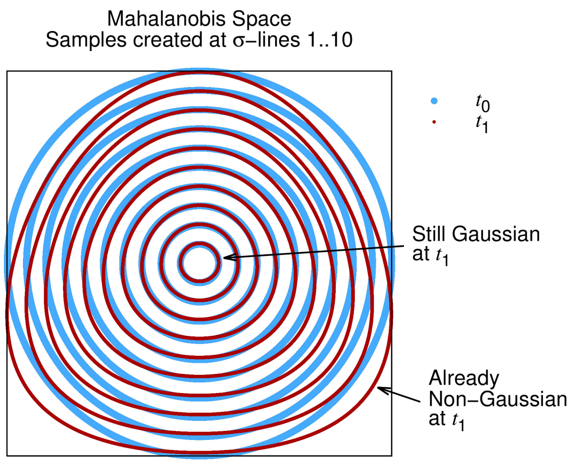

Figure 1. Particles taken at the 1-σ to 10-σ lines before propagation (t_0) and after propagation (t_1). Close to the uncertainty mean, Gaussianity is still intact after propagation while it is no longer given at 10-σ.

The current paper is concerned only with covariance ma-

Proc. 7th European Conference on Space Debris, Darmstadt, Germany, 18–21 April 2017, published by the ESA Space Debris Office
Ed. T. Flohrer & F. Schmitz, (http://spacedebris2017.sdo.esoc.esa.int, June 2017)

trices defined in the cartesian ECI frame. In the next section, confidence intervals in multidimensional space are introduced. In the third section, state-of-the art tests for multivariate normality are briefly explained which go beyond the commonly used Kolmogorov-Smirnov, Cramér-von Mises, and Anderson-Darling tests. The Henze–Zirkler test is then introduced and its applicability to the given problem is assessed by analysing Type I and Type II error rates and how the test results are affected by the number of Monte-Carlo runs and the particle sample size. This is followed by the analysis of when Gaussianity breaks down for different initial variances for objects near GEO. The analysis is based on the simple two-body propagation. It is followed by a brief look at the influence of using a fully numerical propagation tool on the time-frame for which Gaussianity remains intact. The paper concludes with a look at published variances for objects in Earth orbit to give a first impression of how long Gaussianity may remain intact for these.

2. MULTI-DIMENSIONAL CONFIDENCE INTERVALS

The confidence intervals for the single Gaussian are well known: Assuming that the state of an observed object is defined completely in one-dimensional space, the likelihood that it is located within the $\pm 1\,\sigma$, $\pm 2\,\sigma$ or $\pm 3\,\sigma$ intervals is 68.3 %, 95.4 % and 99.7 %, respectively. For two-dimensional space, samples which are within a given interval in one dimension, may still fall outside the same interval in the other dimension. The chance of the object residing within the $\pm 1\,\sigma$ interval in two dimensions for instance reduces from 68.3 % to merely 39.3 %. The confidence intervals can be computed using the χ^2 (Chi-squared) distribution. Its probability *density* function is described by

$$\chi^2(x;k) = \begin{cases} \frac{x^{((k/2)-1)}e^{-x/2}}{2^{k/2}\Gamma(k/2)}, & x > 0; \\ 0, & \text{otherwise} \end{cases} \tag{1}$$

where k is the degrees of freedom, x is the variance and $\Gamma(k/2)$ is the Gamma-function. Here, k takes on integer values and – unlike in the categorical χ^2 test for independence – is equal to the dimensions of the sample space. The parameter x in our case is the variance, σ^2. Table 1 gives an overview of confidence intervals for multidimensional Gaussians for relevant cases which are outlined in the following sections.

2.1. Position only

In the simplest case we are only concerned with an object's position at one instance in time. Only the three-dimensions of space are required and searching the $\pm 3.8\,\sigma$ space in all three dimensions yields a 99.7 % chance of one finding the object.

Table 1. Standard deviation σ at given confidence intervals.

	σ at given Confidence Level		
k	68.2 %	95.5 %	99.7 %
1	1.0	2.0	3.0
2	1.5	2.5	3.4
3	1.9	2.8	3.8
4	2.2	3.1	4.0
5	2.4	3.4	4.3
6	2.7	3.6	4.5
7	2.9	3.8	4.7

2.2. Position prediction

If we want to predict the position of an object at a different time with a certain confidence, the situation changes. Now, we must not only take its current position, but also its position change rate and other parameters such as ballistic coefficient into account which have an effect on its position at another time. Assuming the simplest case without perturbing forces, we can use six dimensions: three for position and three for velocity. As soon as we account for drag or radiation pressure, the ballistic parameter or radiation pressure coefficient may be included. Realistically, we will be using at least seven dimensions. In this case, to predict the object's position with a 99.7 % confidence, the initial sample space up to $\pm\ 4.7\,\sigma$ must be accounted for.

2.3. Manoeuvres & Measurement Errors

As soon as the orbit determination includes additional parameters such as manoeuvres or station biases for instance, the covariance space dimensions may quickly increase, requiring the sample space to be extended.

2.4. Process Noise

None of these cases take into account variations and uncertainties in the prediction of the perturbing forces themselves. These affect the object's state evolution during the prediction interval.

3. TEST FOR MULTIVARIATE NORMALITY

Mecklin and Mundfrom [7] performed a large scale comparison of 13 different tests for multivariate normality (MVN). They split MVN tests into four categories:

- Graphical and correlational approaches
- Skewness and kurtosis approaches

- Goodness-of-fit approaches, and
- Consistent approaches.

The well known Kolmogorov-Smirnov, Cramér-von Mises, and Anderson-Darling test all fall into the category for “Goodness-of-fit approach”. Among the selected methods was an extension of the Anderson-Darling test published by Romeu, J., Oztur, A. [11] which is given the name Romeu–Ozturk test. The Henze–Zirkler [4] test falls into the category of “Consistent approaches”. *Consistent* is used to indicate that it has been mathematically shown that the test will – at least in theory – consistently reject *all* non-MVN distributions. An example of tests of the category “Skewness and kurtosis approaches” are approaches based on the work of Mardia [6]. Among the criteria which the authors used to assess the tests was the rate of Type I[1] and Type II[2] errors as well as feasibility for implementation and desirable mathematical properties. The two major conclusions of this analysis were: a) No single test for MVN delivered perfect results and it was recommended to employ multiple methods for testing of MVN where possible; and, b) If only one test is used, the Henze–Zirkler was recommended. The Romeu–Ozturk was rejected early on in the study due to high Type I type error rates which in some cases exceeded 10 %. These results are supported by a later study by Farrell et al. [2]. In these publications, particle sample sizes were varied between 25 and 250 and sample space dimensions of up to 10 were considered. Based on these results, the Henze–Zirkler test was selected.

3.1. Implementing the Henze–Zirkler Test

The test is implemented based on its original publication [4]. The use of the log-normal probability distribution as per [12] is considered as alternate method for evaluating the Henze–Zirkler test statistic HZ. The basic parameters which are required are:

- $\vec{x}_i$ - particles representing the probability density function
- n_p - particle sample size
- d - dimension of vectors $\vec{x}_i$ (= dimension of sample space)

First, the sample covariance matrix $\boldsymbol{S}$ for the given particle cloud is calculated. This in turn requires the vector containing the sample means $\vec{\bar{x}}$ to be determined:

$$\vec{\bar{x}} = \frac{1}{n} \sum_{i=1}^{n} \vec{x}_i \tag{2}$$

[1]Type I error: An MVN distributed sample is incorrectly identified as being non-MVN distributed.

[2]Type II error: A non-MVN distributed sample is mistakenly identified as being MVN distributed.

The sample mean is also known as the first moment of the sample probability density function. The second moment, the variance, which is represented by the sample variance-covariance matrix in the multi-variate case, is then determined:

$$\boldsymbol{S} = \frac{1}{n} \sum_{i=1}^{n} \left(\vec{x}_i - \vec{\bar{x}}\right) \cdot \left(\vec{x}_i - \vec{\bar{x}}\right)^T \tag{3}$$

The inverse $\boldsymbol{S}^{-1}$ of the covariance (‘dispersion’) matrix must then be found. This can be done efficiently using for instance the *Cholesky-Decomposition* and succinctly inverting its lower triangular decomposition to obtain $\boldsymbol{S}^{-1}$. This method works only for symmetric, positive definite matrices like covariance matrices. An implementation is readily available for instance in Press et al. [10]. With this achieved, everything is available to calculate the test statistic HZ:

$$\begin{aligned} HZ &= \left[\frac{1}{n}\sum_{i=1}^{n}\sum_{j=1}^{n} e^{-\frac{\beta^2}{2}D_{ij}}\right] \\ &\quad - \left[2\left(1+\beta^2\right)^{-\frac{d}{2}} \sum_{i=1}^{n} e^{-\frac{\beta^2}{2(1+\beta^2)}D_i}\right] \\ &\quad + \left[n\left(1+2\beta^2\right)^{-\frac{d}{2}}\right] \end{aligned} \tag{4}$$

Herein D_i gives the squared Mahalanobis distance of the i^{th} observation to the centroid and D_{ij} gives the Mahalanobis distance between i^{th} and j^{th} observations:

$$D_{ij} = \left(\vec{x}_i - \vec{x}_j\right)^T \boldsymbol{S}^{-1} \left(\vec{x}_i - \vec{x}_j\right) \tag{5}$$

$$D_i = \left(\vec{x}_i - \vec{\bar{x}}\right)^T \boldsymbol{S}^{-1} \left(\vec{x}_i - \vec{\bar{x}}\right) \tag{6}$$

The test statistic HZ is small when the particles are MVN distributed and increases with deviation from MVN. The only remaining parameter which has not been defined is β. Henze and Zirkler [4] present an equation to estimate this value based on the particle sample size n_p and sample space dimensions d:

$$\beta = \frac{1}{\sqrt{2}} \left(\frac{n\,(2d+1)}{4}\right)^{\frac{1}{d+4}} \tag{7}$$

3.2. Testing the Null-Hypothesis

Henze and Zirkler [4] and Trujillo-Ortiz [12] propose different methods for testing the null-hypothesis H_0. Both take advantage of the fact that the test-statistic HZ is approximately log-normally distributed. HZ is thus evaluated by comparing where the result falls compared to the log-normal distribution with mean $\hat{\mu}$ and standard deviation $\hat{\sigma}$. These in turn depend only on the sample space dimensions d and β. Different formulations are given by different authors. Henze and Zirkler [4] define them as:

$$\hat{\mu} = 1 - a^{-\frac{d}{2}}\left[1 + \frac{d\beta^2}{a} + \frac{d\,(d+2)\,\beta^4}{2a^2}\right] \quad (8)$$

$$\begin{aligned}\hat{\sigma}^2 = {} & 2\left(1+4\beta^2\right)^{-\frac{d}{2}} \quad (9)\\ & +2a^{-d}\left[1 + \frac{2d\beta^4}{a^2} + \frac{3d\,(d+2)\,\beta^8}{4a^4}\right]\\ & -4w_\beta^{-\frac{d}{2}}\left[1 + \frac{3d\beta^4}{2w_\beta} + \frac{d\,(d+2)\,\beta^8}{2w_\beta^2}\right]\end{aligned}$$

with $a = 1 + 2\beta^2$ and $w_\beta = \left(1+\beta^2\right)\left(1+3\beta^2\right)$.

Henze and Zirkler [4] approximate the critical p-quantile ($p = 1 - \alpha_0$), based on the chosen value for β, the sample space dimensions d and the significance level α_0:

$$q_{\beta,p}(1-\alpha_0) = \mu_{\beta,p}\left(1 + \frac{\sigma^2_{\beta,d}}{\mu^2_{\beta,d}}\right)^{-\frac{1}{2}} \quad (10)$$
$$\times\left(\Phi^{-1}(1-\alpha_0)\sqrt{\log_n\left(1 + \frac{\sigma^2_{\beta,d}}{\mu^2_{\beta,d}}\right)}\right)$$

where Φ^{-1} is the inverse of the standard normal *cumulative* distribution function (also known as the *probit function* and commonly denoted as z_p) and can be calculated using the inverse error function:

$$\Phi^{-1}(r) = \sqrt{2}\cdot\left(\text{erf}^{-1}\left(2\,r - 1\right)\right), \qquad r \in (0,1) \quad (11)$$

The null-hypothesis H_0 being that the sample is indeed MVN distributed is then tested:

$$\begin{aligned} HZ &> q_{\beta,p}(1-\alpha_0) \quad \Rightarrow \quad H_0 \text{ should be rejected}\\ HZ &\leq q_{\beta,p}(1-\alpha_0) \quad \Rightarrow \quad H_0 \text{ cannot be rejected}\end{aligned}$$

If H_0 is rejected, the sample is not MVN distributed. If it cannot be rejected, the sample is assumed to be MVN distributed.

Trujillo-Ortiz [12] initially calculates the log-*normalised* mean $\hat{\mu}$ and standard deviation $\hat{\sigma}$ which are correctly defined by the following equations:

$$\hat{\mu} = \ln\left(\sqrt{\frac{\mu^4}{\sigma^2 + \mu^2}}\right) \quad (12)$$

$$\hat{\sigma} = \sqrt{\ln\left(\frac{\sigma^2+\mu^2}{\mu^2}\right)} \quad (13)$$

The significance level is then calculated from the cumulative lognormal distribution:

$$\alpha = 1 - lognormal\left(HZ, \hat{\mu}, \hat{\sigma}\right) \quad (14)$$

The *lognormal* can be expressed via the error function **erf** which in turn can be calculated using the incomplete *lower* gamma function $\gamma(k = 0.5, r)$. Resolving this chain leads to the implementation:

$$lognormal\left(HZ, \hat{\mu}, \hat{\sigma}\right) = \quad (15)$$
$$\begin{cases} 0.5\cdot\left(1 - \gamma\left(0.5, x^2_{HZ,\hat{\mu},\hat{\sigma}}\right)\right), & x > 0.0\\ 0.5\cdot\left(1 + \gamma\left(0.5, x^2_{HZ,\hat{\mu},\hat{\sigma}}\right)\right), & x \leq 0.0\end{cases}$$

where, $x()$ is given by:

$$x\left(HZ, \hat{\mu}, \hat{\sigma}\right) = -\frac{1}{\sqrt{2}}\cdot\frac{\ln\left(HZ\right) - \hat{\mu}}{\hat{\sigma}} \quad (16)$$

These results will be denoted α as they provide the level of significance as test metric. Finally, the test for MVN becomes:

$$\begin{aligned}\alpha &> 0.05 \quad \Rightarrow \quad H_0 \text{ cannot be rejected}\\ \alpha &\leq 0.05 \quad \Rightarrow \quad H_0 \text{ should be rejected}\end{aligned}$$

3.3. Mahalanobis Space

For visualisation purposes, the particle cloud is represented in *Mahalanobis space*. Within this space the distance of any particle from the sample mean is represented in multiples of the standard deviation. The transformation by which this is achieved is a so called "whitening" transformation which can be performed in different ways. Here, the inverse lower triangular matrix $\boldsymbol{L}^{-1}$ of the sample covariance matrix $\boldsymbol{S}$ obtained through the Cholesky decomposition is used. It is simply multiplied with the vector pointing from the sample mean to the particle whose base is to be transformed:

$$\Delta\vec{y}' = \boldsymbol{L}^{-1}\Delta\vec{y} \quad (17)$$

3.4. Type I and Type II Error

The quality of the test is determined by assessing Type I and Type II error rates. Simulation results which quantify both are given in [2, 4, 7]. Within these publications, a multitude of multivariate distributions was used as basis for the particle samples for assessing Type II error rates. Across the publications particle sample sizes ranged from 20 to 250 and sample space dimensions ranged from two to 10. Type I error was found to occur in three to six percent of the simulation runs. Type II error rates depended heavily on the multivariate distribution from which the particles were created.

Here, the Type I and Type II error rate is assessed for particle sample sizes of 10^2, 10^3 and 10^4. Type I error is simply assessed at $t0$ without propagation. Type II error is assessed at $t0$ + 100 orbits where the distribution can

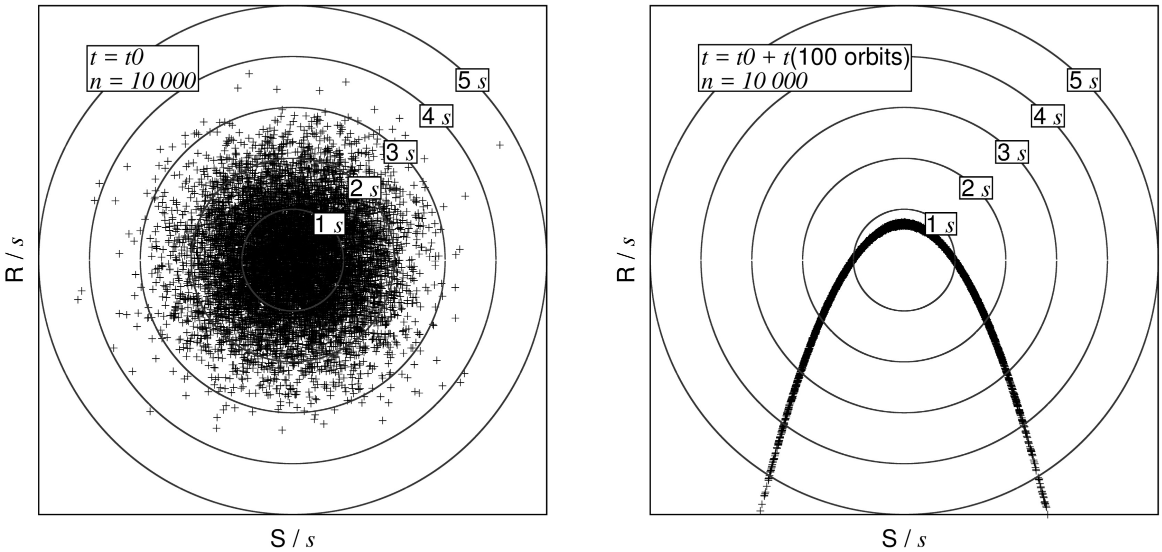

Figure 2. Particle distribution with a particle sample size of 10 000 at the initial epoch (left) and 100 orbits later (right) in Mahalanobis Space. The units s are the sample standard deviations. The coordinates R and S are radial and along-track directions within the object centred RSW frame and give the orientation of the depicted particle clouds to the first order. The true orientation of the coordinates of the Mahalanobis Space are generated as part of the process of transformation from ECI and may differ slightly from these depending on the make-up of the particle distribution.

safely be assumed to be non-Gaussian. Later simulations will aim at detecting small deviations from Gaussianity within the first couple of orbits. For the testing of the Type II error rate, an obviously non-Gaussian distribution is preferred which exhibits the dominant characteristics associated with uncertainty volume deformation we are concerned with. For each particle sample size, 1 000 samples are computed and evaluated. The random number generator implementation of the Mersenne Twister of the C++ library `<random>` is seeded with values between one and 1 000 to create the particle samples. To account for possible errors stemming from the coordinate transformations within the simulation environment, the samples undergo the following steps before their distribution is tested for multivariate normality:

1. Creation based on covariance matrix in ECI
2. Conversion to Equinoctial elements
3. Conversion back to ECI
4. MVN testing.

The conversion to Equinoctials is included as this is the frame within which the two-body propagation operates (see Section 4.4). The state $\vec{s}_0 = (x, y, z, \dot{x}, \dot{y}, \dot{z})$ in ECI coordinates with position in meters and velocity in meters per second for the simulation is:

$$\vec{s}_0 = (42163960.6, 0, 0, 0, 3074.66772, 0) . \tag{18}$$

and the covariance matrix is a purely diagonal matrix where the position and velocity variances are taken as

$$\begin{aligned} \sigma_x^2 = \sigma_y^2 = \sigma_z^2 = 10^5\ \text{m}^2 \\ \sigma_{\dot{x}}^2 = \sigma_{\dot{y}}^2 = \sigma_{\dot{z}}^2 = 10^{-3}\ \text{m/s}^2 \end{aligned} \tag{19}$$

To visualise the distributions used for the Type I and Type II error testing, Figure 2 presents the particle distribution with a particle sample size of 10 000 at the initial epoch and 100 orbits later in Mahalanobis space in the orbital plane. The curved distribution in the right hand plot clearly shows the departure from Gaussianity.

Table 2 shows the percentage of tests in which a normally distributed particle cloud was incorrectly flagged as being non-normally distributed (Type I) and the percentage of tests in which the non-normally distributed particle cloud was incorrectly flagged as being normally distributed (Type II). The results for the Type I error is consistent with the values published by [2, 4, 7]. For **Type I** errors, two things can be observed: 1) The results even for the smallest particle sample size of 25 is accurate and robust. 2) The error rate seems to increase slightly for larger particle sample sizes. For **Type II** error rates, non-normality is detected in most cases for a particle sample size of 50 and in all cases for a particle sample size of 100. Across all simulations, the results for the two test statistics is identical to within the first decimal place.

Table 2. Type I and Type II error rate of Henze–Zirkler test. Values are given in percent of simulation runs.

Sample Size	Simulations / % HZ	α
Type I Error Rates (t_0)		
25	4.8	4.8
50	3.4	3.4
100	4.8	4.8
1 000	4.4	4.4
10 000	5.1	5.1
Type II Error Rates ($t0$ **+ 100 orbits)**		
25	44.2	44.2
50	1.6	1.6
100	0.0	0.0
1 000	0.0	0.0
10 000	0.0	0.0

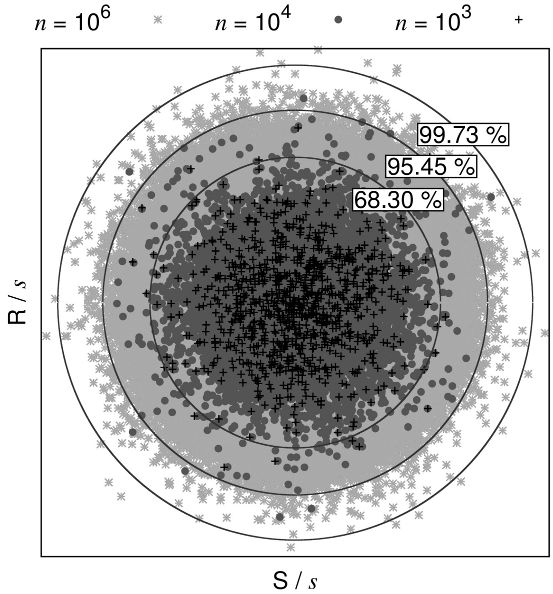

Figure 3. Particle distribution in Mahalanobis space at initial epoch with confidence interval lines in orbital plane components superimposed.

4. SIMULATION SETTINGS

Careful definition of particle sample size and number of Monte-Carlo runs is required to obtain meaningful results for the breakdown of Gaussianity. This is performed first, followed by the definition of initial orbits and initial covariances to be analysed. The propagation schemes are outlined succinctly.

4.1. Sample Size

With increasing particle sample size, the chance of creating particles further away from the mean increases. As was outlined in the introduction and visualised by Figure 1, propagating the uncertainty space would cause Gaussianity to break down at the instance directly after the initial epoch. The upper limit can be defined by prudently choosing a confidence level beyond which unneeded or unusable accuracy would be generated. The lower limit is given by the requirement of covering a large enough interval to be certain to a defined level, that the object future position is contained in the solution.

The dependence of the space being sampled on the particle sample size is visualised in Figure 3. The plot depicts the distribution of the particles in Mahalanobis space within the orbital plane. *It must be noted, that even particles which fall within the* $1\ s$ *region in this representation may be outside of the* $1\ s$ *region in any of the other parameters not shown here.*

Here it is assumed that the volume contained in the probability density function outside of the 99.7 % confidence region has negligible impact on any useful applications of the uncertainty volume. The lower limit is given by the necessity to create a significant number of particles up to the limits of that level. To assess a sample with regards to these two limits, the number of particles which are outside of the 99.7 % are counted and the number of particles which are in between the 99.7 % and the 95.45 % confidence interval are counted. This is done by calculating the magnitude of each particle vector in Mahalanobis space by simply taking the square root of the position and velocity components squared (in the two-body case, only six parameters define the state fully). The results are given in Table 3. The table offers a surprising result in that it shows that particle sample sizes above 10 000 already create a significant number of particles which are outside of the upper limit defined by the 99.7 % confidence interval. In statistics any sample size below 30 is typically regarded as being too low to hold significance [1]. The particle sample size of 10 000 contains less than 11 particles (average value from 100 simulations) beyond the upper limit and many more in the interval just below and is therefore chosen for the current investigation.

Table 3. Number of particles within the 95.45 % and 99.7 % confidence interval and outside of the 99.7 % confidence interval.

Sample Size	95.45 % – 99.7 %	$>$ 99.7 %
10^7	239 435	11 709
10^6	23 812	1 168
10^5	2 380	104
10^4	**237**	**11**
10^3	22	1

Table 4. Size of 95.5 % confidence interval for particle sample size $n_p = 10\,000$. The second column is the interval of possible results. The third column shows the decision threshold value for MVN.

	Result Interval	Decision Threshold	# of MC runs 10	100
HZ	]0,∞[	1.00	0.024	0.007
α	[0,1]	0.05	0.33	0.10

4.2. Monte-Carlo Runs

The number of Monte-Carlo runs influences the stability of the simulation results. To visualise the effect, a particle sample size of $n_p = 100$ suffices. Three simulation settings are tested: 100, 1 000 and 10 000 Monte-Carlo runs (= n_{mc} = "Monte-Carlo sample size"). Each Monte-Carlo simulation is performed 100 times, each time with a different randomiser seed. The resulting behaviour is described by the *Central Limit Theorem* (CLT). Applied to our case, the CLT states that the histogram of the mean values from the 100 Monte-Carlo simulations will be normally distributed regardless of the probability distribution they were computed with. Furthermore, the CLT offers a simple equation of estimating the standard deviation of the sample means $\sigma_{\bar{x}}$:

$$\sigma_{\bar{x}}(n_{mc}) = \frac{s(n_{mc})}{\sqrt{n_{mc}}} \tag{20}$$

$s(n_{mc})$ is the sample standard deviation from a single Monte-Carlo simulation and n_{mc} is the number of Monte-Carlo simulations used to obtain it. The results for the determined sample means of each of the three sets for the α test statistic are depicted in Figure 4 with the result of the CLT superimposed. Results for the HZ test are omitted as they do not provide additional insight. It can be seen that the CLT offers a powerful tool in estimating a sensible number of Monte-Carlo runs if requirements are well defined.

For the defined particle sample size of 10 000, simulations with 10 and with 100 Monte-Carlo runs are performed. Table 4 shows the size of the interval wherein a simulation will fall with 95.5 % confidence based on the CLT (interval given by $\pm(2 \times 1\,\sigma_{\bar{x}})$). For α, the range of values within which MVN is defined is]0.05,1]. For $n_{mc} = 100$, α will remain within a range spanning more than 10 % of this interval in 95.5 % of the cases. Although this variation is still quite high, going to even larger n_{mc} is computationally too expensive in the current openMP based implementation.

4.3. Initial Orbits and Covariances

The initial orbit used for the current assessment is given in Table 5. Table 6 shows the settings for the initial variances. No initial covariances are assumed. The variances

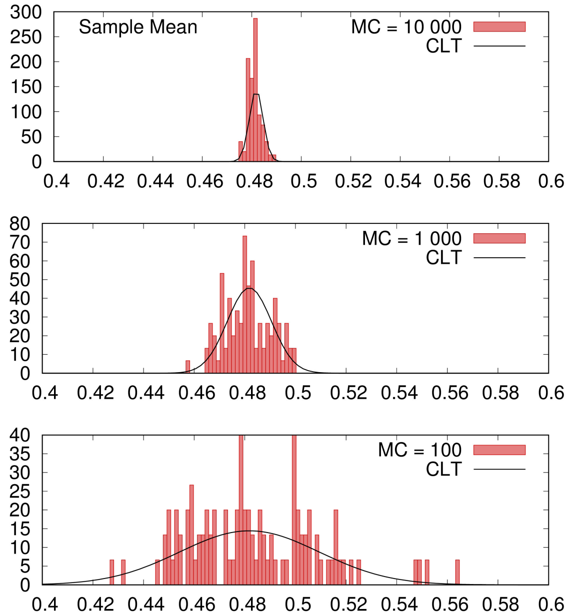

Figure 4. Impact of the number of Monte-Carlo runs on a simulation with particle sample size n_p = 100 at $t0$. The figure shows the distribution of mean values for the $\alpha_{lognormal}$ statistic where each of the three Monte-Carlo settings 100 (bottom), 1 000 (middle) and 10 000 (top) has been performed 100 times, with varying randomiser seeds. The result from the Central Limit Theorem are superimposed where the mean value is 0.482 and the sample standard deviation for the three Monte-Carlo sample sizes are $s_{100} = 0.2763$, $s_{1\,000} = 0.2766$ and $s_{10\,000} = 0.2769$.

are given in the RSW frame where R points in the radial, W in the cross-track, and S in the along-track direction. Due to the negligible eccentricity of the orbit, the frame is synonymous to the NTW frame. Two sets, set *Cx1* and set *Cx2*, with three variance settings each are simulated here. Set *Cx1* has the largest uncertainties in along-track and identical uncertainties in the cross-track and radial directions. Set *Cx2* uses the same values however with the largest uncertainties in radial direction. This variation helps to gain insight into the effect of variances in different directions in the object centered frame. Variances for velocity are nine orders of magnitude smaller in the largest of the three uncertainty directions and seven orders smaller in the other two directions. Case *C3a* is roughly based on average orbit determination results using optical measurements of geostationary spacecraft. It is however by no means representative as uncertainties in individual directions will vary greatly between objects, observations and based on the specifics of the orbit determination method applied. The cases *C2y* and *C1y* successively reduce all variances equally by two orders of magnitude. Investigating small variances is of interest when assessing the effect improvements in the orbit determination process may have as well as understanding how ephemeris from operators of spacecraft may be expected compare.

Table 5. Overview of initial Keplerian orbit elements.

Parameter	Unit	Value
a	km	42163.9606
e	–	5×10^{-10}
i	$\circ$	0.0
Ω	$\circ$	0.0
ω	$\circ$	180.0
ν	$\circ$	180.0

Table 6. Overview of initial covariances in RSW frame. R = radial; W = cross-track; S = W × R = along-track

ID	Variances					
	x_R	x_S	x_W	$\dot{x}_R$	$\dot{x}_S$	$\dot{x}_W$
		m^2			$\mathrm{m}^2\,\mathrm{s}^{-2}$	
C1a	10^{-2}	10^{1}	10^{-2}	10^{-9}	10^{-8}	10^{-9}
C2a	10^{0}	10^{3}	10^{0}	10^{-7}	10^{-6}	10^{-7}
C3a	10^{2}	10^{5}	10^{2}	10^{-5}	10^{-4}	10^{-5}
C1b	10^{1}	10^{-2}	10^{-2}	10^{-8}	10^{-9}	10^{-9}
C2b	10^{3}	10^{0}	10^{0}	10^{-6}	10^{-7}	10^{-7}
C3b	10^{5}	10^{2}	10^{2}	10^{-4}	10^{-5}	10^{-5}

4.4. Orbit Propagation

Two-body Propagation Two-body propagation is performed in Equinoctial elements using the Mikkola/Halley 4 method as described by [8] with an Erratum to the equation of the Mikkola starter value as per [9]. In the current implementation, this method shows accuracy at GEO altitude for eccentricities below 0.800 of better than 0.001 mm and better than 20 mm for eccentricities between 0.8000 and 0.9998.

Numerical Propagation Using an extended force model instead of the simplistic two-body propagation will lead to a quickening of the breakdown of Gaussianity. To get a first impression of this effect, the General Mission Analysis Tool (GMAT) version R2015a is employed. Standard input parameters are used which lead to an area-to-mass ratio for a spherical object of about 0.001. No drag is used due to the high altitude being investigated. Integration is performed using the Runge-Kutta-89 method. The EGM-96 Earth Gravity Model is used to degree and order 30. Third body gravity effects from the Sun and Moon are taken into account.

5. TWO-BODY RESULTS

5.1. Effect of Sample Size

The particle sample size effect on the epoch at which the breakdown of Gaussianity is detected is exemplified in Figure 5 based on two simulations and using the α metric. Results for the HZ metric are not shown as they are qualitatively identical and quantitatively almost the same and will be discussed in the following sections. Simulation 1 uses $n_p = 10\,000$ and $n_{mc} = 100$. Simulation 2 uses $n_p = 100$ and $n_{mc} = 10\,000$. Both simulations assume the initial GEO given in Table 5 and initial variances as per Table 6, case C1a. Given the initial conditions, the variances are largest in the along-track. The difference in Monte-Carlo runs between the two simulations affects the stability of the median of the simulations. It follows that the median from simulation 2 has a much higher likelihood of being close to the actual median for $n_p = 100$ than the result of simulation 2 will have of being close to the median for $n_p = 10\,000$. The results are represented by the median, the area enclosed by $\pm 25\,\%$ of the runs (= first and third quartile) relative to the median and the extent of all results for both simulations. The median and quartiles are preferred to the mean and standard deviation for assessing the results because at values close to zero, the standard deviation extends to negative values in α which are mathematically meaningless. The time until the breakdown of Gaussianity differs by about a factor two. Even during the timeframe where the median and first quartile are well above the hypothesis rejection level of $\alpha_0 = 0.05$, some simulations will result in a Type I error. This is consistent with the findings of Section 3.4 where it was shown that a Type I error should be expected in about 5 % of the simulations which is a major reason behind performing Monte-Carlo simulations.

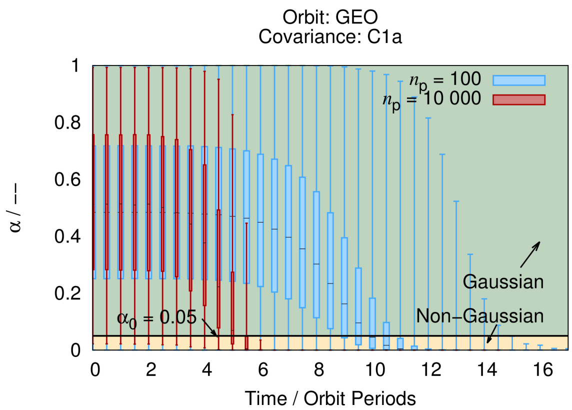

Figure 5. The sample size affects the extent of the uncertainty space being sampled. Large sample sizes cover a larger area, becoming non-normally distributed more quickly. The median, first and third quartile and maximum values from all simulations are shown for sample sizes $n_p = 100$ and $n_p = 10\,000$. The null-hypothesis that particles are MVN distributed is rejected for values below $\alpha = \alpha_0 = 0.05$.

5.2. Effect of Monte-Carlo Runs

The effect of the number of Monte-Carlo runs from which the epoch at which the breakdown of Gaussianity is derived is detected is exemplified by comparison of two simulations. Initial orbit as per Table 5 and diagonal variances as per Table 6, case C2b are used. Simulation 1 employs $n_{mc} = 100$ and simulation 2 $n_{mc} = 10\,000$. Although differences are obvious for the two simulations, the median values for both are within 0.1 orbit periods of one another. Due to the larger number of simulations performed, the range of values is larger for $n_{mc} = 10\,000$.

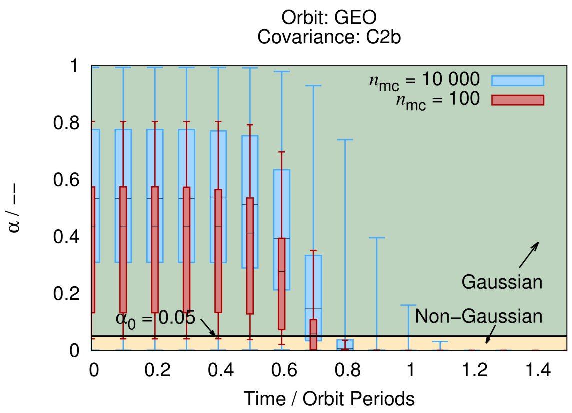

Figure 6. Effect of Monte-Carlo runs on epoch of breakdown of Gaussianity. Comparison of $n_{mc} = 100$ and $n_{mc} = 10\,000$ for $n_p = 10\,000$ and initial conditions as per Tables 5 and 6.

5.3. Effect of Variances

Figure 7 compares the breakdown of Gaussianity for the two-body case given the detailed simulation settings. Each plot compares the evolution of the variance based on a *Cxa* case with the largest uncertainty in along-track to the results of the respective *Cxb* case with the same variances values however with the largest uncertainty in the radial direction. The plots on the left hand side provide the α-metric while the plots on the right-hand side show the results using the HZ-metric for the same simulations.

Test metric comparison The results of the α and HZ metric show almost identical epochs for the breakdown of Gaussianity. The major difference between the two is essentially that once the distribution becomes non-Gassian, the α metric reduces to zero and no additional information can be gleaned from the result. The HZ metric on the other hand increases with growing divergence from Gaussianity and thus offers slightly more information in this region. Visually, the α metric is slightly easier to interpret.

Large along-track vs. large radial uncertainties In the case where the larger uncertainty is in along-track direction, the Gaussian assumption holds for roughly three times longer compared to the case where uncertainty is largest in radial direction. Whether this difference is driven by the position or the velocity uncertainty is not clear and may be analysed in more detail in a future study.

Initial variance size impact As expected, Gaussianity breaks down earliest for the case where initial uncertainties are largest (*C3y*). Interestingly, the time span for Gaussianity seems to double between *C1y* and *C2y* and again between *C2y* amd *C3y*. Six test cases however are too few to allow any exact correlation to be inferred. For the largest uncertainties in the along-track, the longest time frame during which the Gaussian assumption may be applied is about six orbital periods with the first quartile dropping below the rejection threshold at between four and five orbital periods. For the largest initial variances, Gaussianity is only given for about one orbital period (roughly one day). With the largest uncertainties in radial direction, the longest time frame until breakdown of Gaussianity is between 1.5 and two orbital periods. The shortest time frame is less than half an orbital period.

6. EXTENDED FORCE MODEL EFFECT

A fair comparison is only possible, if all two-body simulations are also using the full-force model as outlined in Section 4.4. Here, a first impression is gained of the effect of using an extended force model by comparing the position of 8 000 particles generated along the one to 10-σ lines in the orbital plane after seven orbits. This is the same setup as was used to generate Figure 1. Visually, the two-body solution and the the extended force model solution are almost indiscernible (see Figure 8). A larger deviation should be expected when initial variances are extended to higher dimensions and for objects with high area-to-mass ratios.

7. PUBLISHED COVARIANCES

Flohrer et al. [3] performed an extensive analysis of the position errors in historic TLE. They split TLEs into different categories and estimated the standard deviation in position in RSW coordinates. The category with eccentricity below 0.1 and perigee altitude above 25 000 km focuses on orbits in the GEO region. Between 1990 and 2008, the standard deviation in cross-track direction remained quite constant at about 100 m; values in radial direction varied between 400 m and 700 m and values in along-track varied between 500 m and 800 m. Unfortunately, no analysis of velocity uncertainties was performed. Klinkrad and Martin [5] presented estimated velocity uncertainties for low eccentricity TLE in LEO which are on the order of 500 mm/s in radial and between 100 mm/s and 200 mm/s in along-track and cross-track. These values are three orders of magnitude worse than the ones assumed in the current simulation study. Case *C3a* (Table 6) has the largest along-track standard deviation simulated in the current study and was about 316 m. The

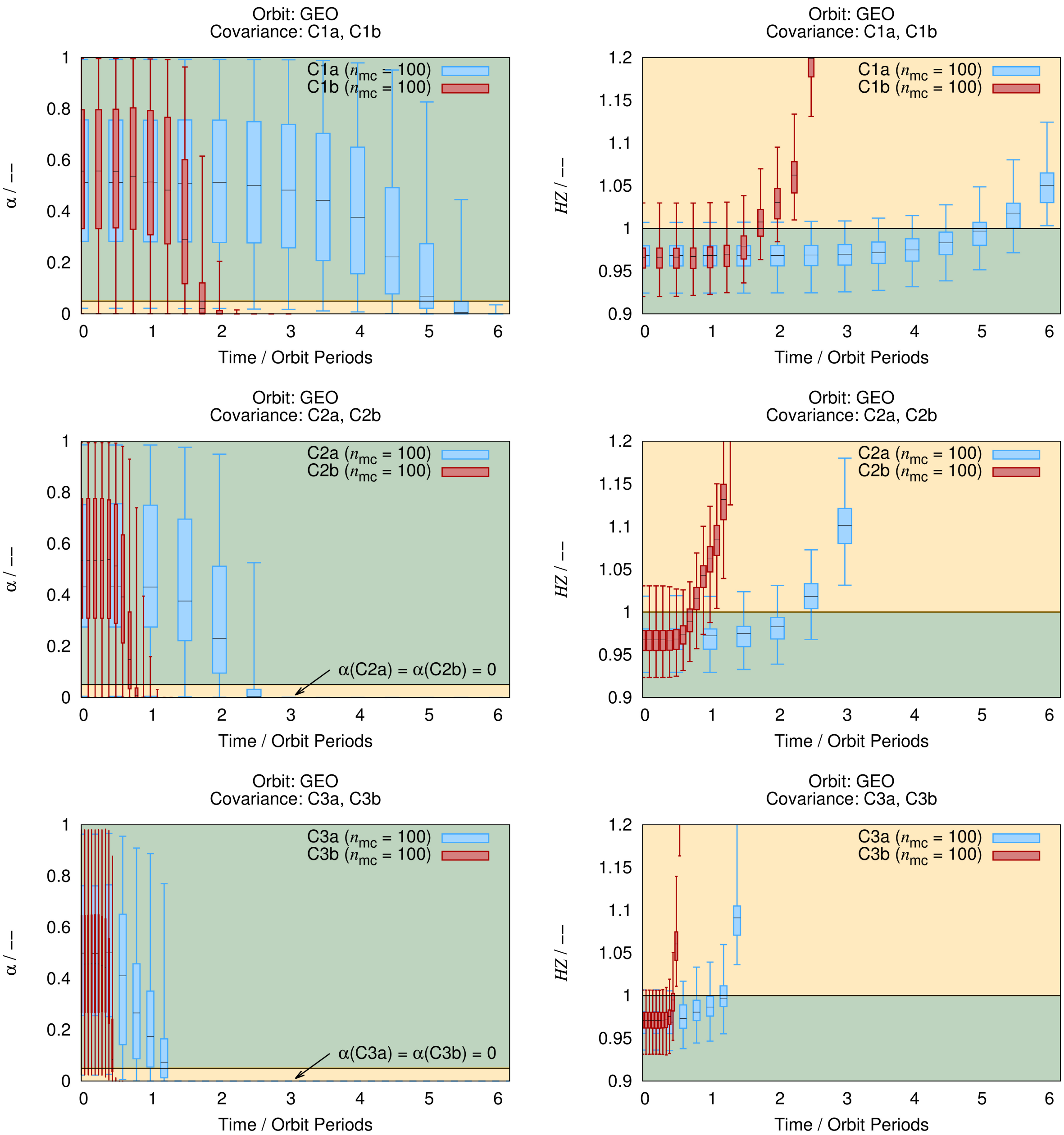

Figure 7. Timeframe until breakdown of Gaussianity using the Henze–Zirkler metric for test cases defined in Tables 5 and 6 for the two-body case.

published cross-track and radial standard deviations are closer to those used in case *C3b*. In these two cases, the uncertainty volume became non-Gaussian within the first 1.5 periods. If the velocity uncertainties given in [5] were used, Gaussianity would break even earlier. Vallado and Alfano [13] states that TLEs are created autonomously and without incorporation of manoeuvres into the orbit determination; assessments of the accuracy of TLEs are therefore good for determining the order of magnitude of uncertainties and how they may vary for different orbit categories.

8. CONCLUSIONS

The current paper addressed the issue of uncertainty volume prediction for Earth orbiting objects. It was shown that the time until the initially Gaussian uncertainty volume becomes non-Gaussian not only depends on the size of the initial variances, but also on the size of the sample space which is assessed. This is especially critical for random particle methods as the Gaussian itself extends to infinity and increasing the sample size also expands the physical extent of the uncertainty volume which is sampled from. To be 99.7 % confident to find the ob-

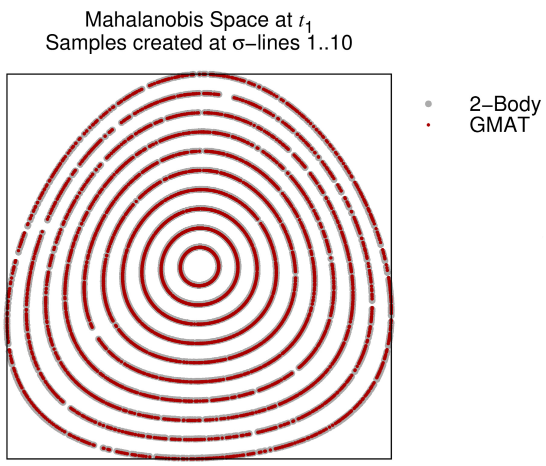

Figure 8. Particles taken at the one to 10-σ lines. Comparison after propagation at t_1 between two-body solution (gray) and full force model using GMAT R2015a (red).

ject at a future epoch based on initial uncertainties alone and assuming a seven-dimensional covariance matrix requires assessing the initial uncertainty volume out to the 4.7 σ level equally in all dimensions. A sample size of 10 000 is found to adequately sample this uncertainty volume. After a review of literature which compares different tests for multivariate normality, the Henze–Zirkler test was chosen and implemented. All tests of the implemented method show good agreement with published values.

The case of a circular geostationary object was assessed based on two-body motion. Six different initial covariance matrices were considered. The uncertainties were defined in cartesian, object centered coordinates. In three of the cases, the largest position and velocity uncertainty was assumed to be in along-track direction. In three other cases, the largest uncertainties were assumed to be in radial direction. In the cases where the largest uncertainties were in the along-track, the longest and shortest time frames for which Gaussianity held was about six orbit periods and about one orbit period respectively. In the cases where the largest uncertainties were in radial direction, the time until Gaussianity broke down was three times shorter.

Perturbations will lead to a shorter timeframe during which the uncertainty volume may be assumed to remain Gaussian compared to the two-body case assessed here. An impression of its effect was gained by comparing the particle positions in Mahalanobis space propagated from positions initially defined along the σ-lines of the uncertainty space to the two-body case. For the simple case of uncertainty only in position within the orbit plane, visual comparison revealed no obvious discrepancies. A more detailed assessment of the effects of using a full numerical force model will be performed in future work.

Position standard deviations from studies of historical TLE data are close to the largest initial uncertainties investigated here; velocity standard deviations are several orders of magnitude worse than the ones assumed here. An uncertainty volume based on these values can be expected to become non-Gaussian within the first orbit.

ACKNOWLEDGMENTS

The authors of this paper wish to acknowledge funding for this research project from the Cooperative Research Centre for Space Environment Management (SERC Limited).

REFERENCES

1. S. Christian Albright, Wayne Winston, and Christopher Zappe. *Data Analysis and Decision Making*. 4 edition, 2011. ISBN 978-0538476126.
2. Patrick J. Farrell, Matias Salibian-Barrera, and Katarzyna Naczk. On tests for multivariate normality and associated simulation studies. *J. Stat. Comput. Simul.*, 77(12):1065–1080, 2007. ISSN 0094-9655. doi: 10.1080/10629360600878449.
3. Tim Flohrer, Holger Krag, and Heiner Klinkrad. Assessment and categorization of TLE orbit errors for the US SSN catalogue. *Risk*, 8(9):10–11, 2008.
4. N. Henze and B. Zirkler. A class of invariant consistent tests for multivariate normality. *Commun. Stat. - Theory Methods*, 19(10):3595–3617, 1990. ISSN 0361-0926. doi: 10.1080/03610929008830400. URL `http://www.tandfonline.com/doi/abs/10.1080/03610929008830400`.
5. Heiner Klinkrad and Clare Martin. *Space Debris - Models and Risk Analysis*. Springer-Praxis Books in Astronautical Engineering, 2006. ISBN 3-540-25448-X.
6. K. Mardia. Measures of multivariate skewness and kurtosis with applications. *Biometrika*, 57:519–530, 1970.
7. Christopher J. Mecklin and Daniel J. Mundfrom. A Monte Carlo comparison of the Type I and Type II error rates of tests of multivariate normality. *J. Stat. Comput. Simul.*, 75(2):93–107, 2005. ISSN 0094-9655. doi: 10.1080/0094965042000193233. URL `http://www.tandfonline.com/doi/abs/10.1080/0094965042000193233`.
8. Daniel L. Oltrogge. Efficient solutions of kepler's equation via hybrid and digital approaches. *The Journal of the Astronautical Sciences*, 62(4):271–297, 2015. ISSN 2195-0571. doi: 10.1007/s40295-015-0078-5. URL `http://dx.doi.org/10.1007/s40295-015-0078-5`.
9. Daniel L. Oltrogge. Erratum to: Efficient solutions of kepler's equation via hybrid and digital approaches. *The Journal of the Astronautical Sciences*, 64(1):97–97, 2017. ISSN 2195-0571. doi:

10.1007/s40295-016-0102-4. URL http://dx.doi.org/10.1007/s40295-016-0102-4.

10. William H. Press, Saul A. Teukolsky, William T. Vetterling, and Brian P. Flannery. *Numerical Recipes in C - The Art of Scientific Computing*. 2 edition, 1997. ISBN 0-521-43108-5.

11. Romeu, J., Oztur, A. A comparative study of goodness-of-fit tests for multivariate normality. *Journal of Multivariate Analysis*, 46:309–334, 1993.

12. Antonio Trujillo-Ortiz, January 1 2009. URL: http://au.mathworks.com/matlabcentral/fileexchange/17931-hzmvntest/content/HZmvntest/HZmvntest.m, accessed on March 23, 2017.

13. David A. Vallado and Salvatore Alfano. Curvilinear coordinate transformations for relative motion. *Celest. Mech. Dyn. Astron.*, 118(3):253–271, 2014. ISSN 09232958. doi: 10.1007/s10569-014-9531-1.